Electronic Supplementary Information

NiS-MoS_2 hetero-nanosheet arrays electrocatalysts for efficient overall water splitting

Shundong Guan,[ab] Xiuli Fu,*[a] Zhezhu Lao,[c] Chuanhong Jin[c] and Zhijian Peng*[b]

[a] *State Key Laboratory of Information Photonics and Optical Communications, and School of Science, Beijing University of Posts and Telecommunications, Beijing 100876, P.R. China)*

[b] *School of Science, China University of Geosciences, Beijing 100083, P.R. China*

[c] *State Key Laboratory of Silicon Materials, School of Materials Science and Engineering, Zhejiang University, Hangzhou, Zhejiang 310027, China*

*xiulifu@bupt.edu.cn. Tel: 86-10-62282242. Fax: 86-10-62282242.

*pengzhijian@cugb.edu.cn. Tel: 86-10-82320255; Fax: 86-10-82322624.

Financial support from the National Natural Science Foundation of China (grant nos. 11674035 and 61274015), and Excellent Ph.D. Students Foundation in Beijing University of Posts and Communications (grant no. CX2018214) is gratefully acknowledged.

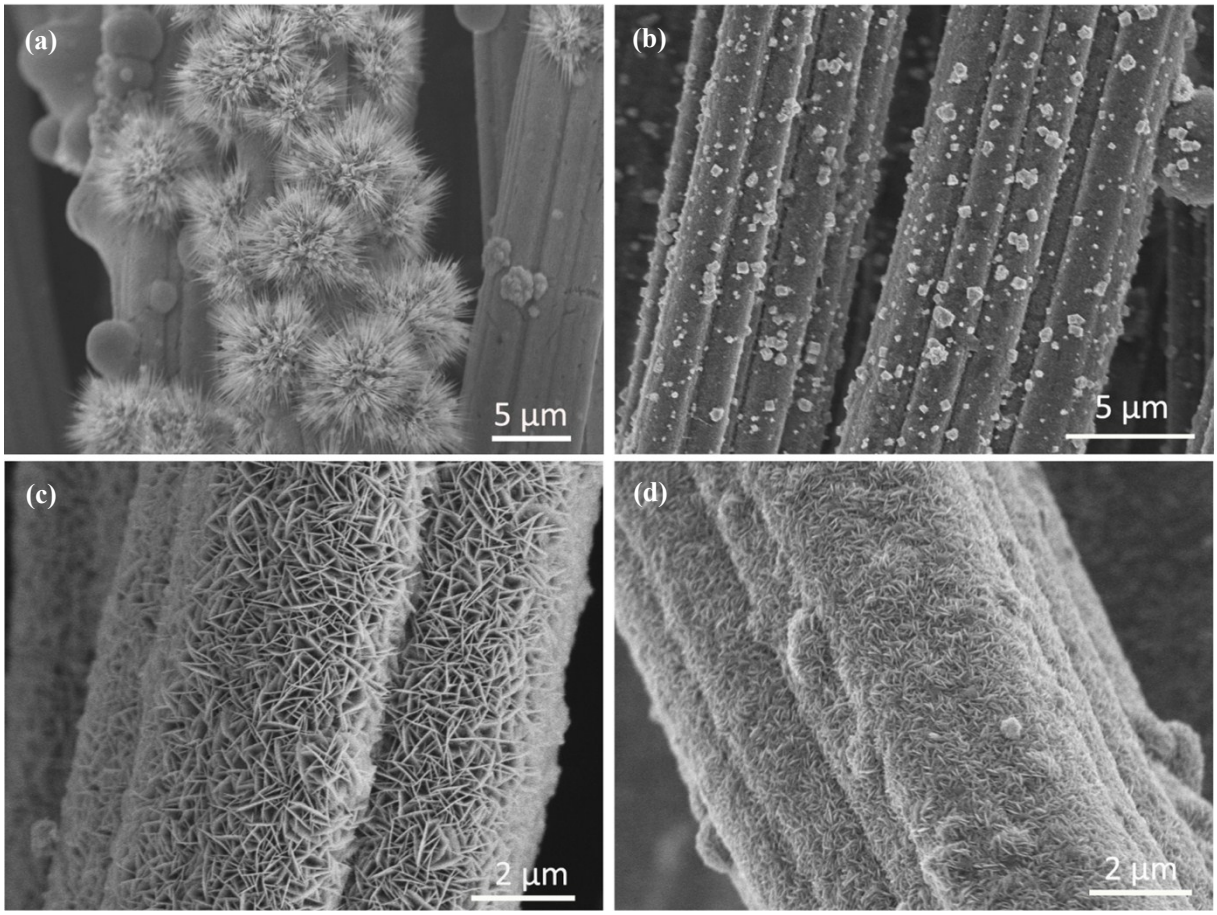

Fig. S1 SEM images of NiS-MoS_2 nanostructures on CC synthesized with different concentrations of sodium dodecyl sulfate (SDS): (a) 0, (b) 0.1, (c) 0.2, and (d) 0.3 mol·L^{-1}.

In order to investigate the function of SDS for the formation of NiS-MoS_2 HNSAs, different concentrations of SDS were used during the hydrothermal synthesis. Without SDS in the solution, some urchin-like nanostructures were formed independently on the CC (**Fig. S1a**), indicating that NiS and MoS_2 couldn't uniformly grow on the surface of CC due to the poor wettability of carbon in aqueous solution. Similarly, when a low concentration (0.1 mol·L^{-1}) of SDS was used, only some nanoparticles were formed, decorating on the CC (**Fig. S1b**). However, when 0.2 mol·L^{-1} SDS was applied, many large nanosheets were uniformly and vertically aligned as nanowalls on the CC (**Fig. S1c**). By further increasing the concentration of SDS to 0.3 mol·L^{-1}, the formed nanosheets were aggregated together but had a smaller size (**Fig. S1d**). Thus, 0.2 mol·L^{-1} of SDS was optimized for the synthesis of NiS-MoS_2 HNSAs.

Shundong Guan, et al., *Sustainable Energy & Fuels*, Fig. S2

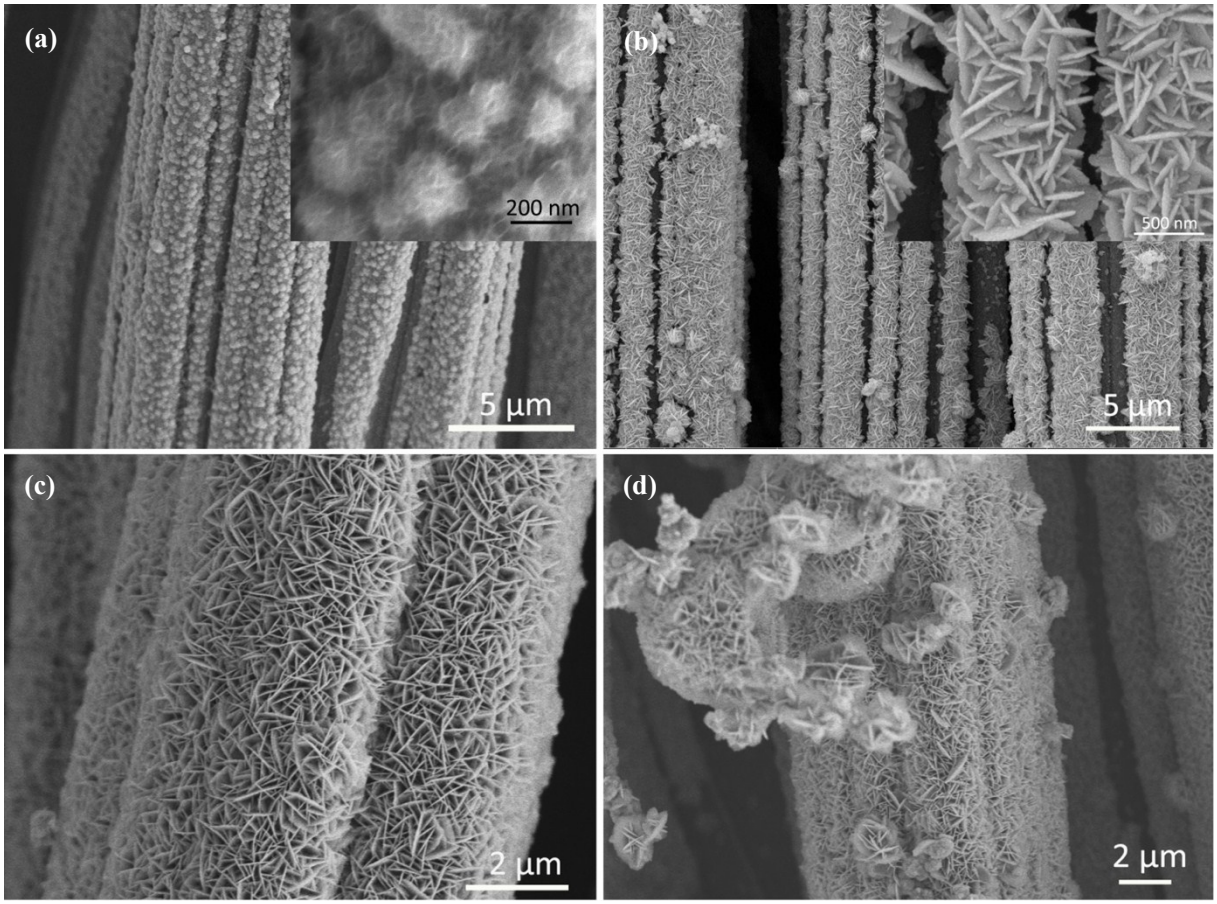

Fig. S2 SEM images of NiS-MoS_2 nanostructures on CC synthesized at 180 ˚C for different times: (a) 4, (b) 6, (c) 9 and (d) 12 h. The insets in (a) and (b) are their corresponding high-magnification SEM images, respectively.

As is seen in **Fig. S2a**, after 4 h hydrothermal reaction, many flower-like nanosheets have formed on the surface of CC. These tiny-flowers would continually grow larger and interconnect with each other with the extension of reaction time, and wall-like nanosheets with higher thickness appeared (**Fig. S2b**). After 9 h reaction, the optimized NiS-MoS_2 HNSAs with large size were obtained (**Fig. S2c**). By further extending the reaction time to 12 h, more of large-sized flower-like NiS-MoS_2 hierarchical nanostructures would separately grow onto the as-formed nanosheets array (**Fig. S2d**).

Shundong Guan, et al., *Sustainable Energy & Fuels*, Fig. S3

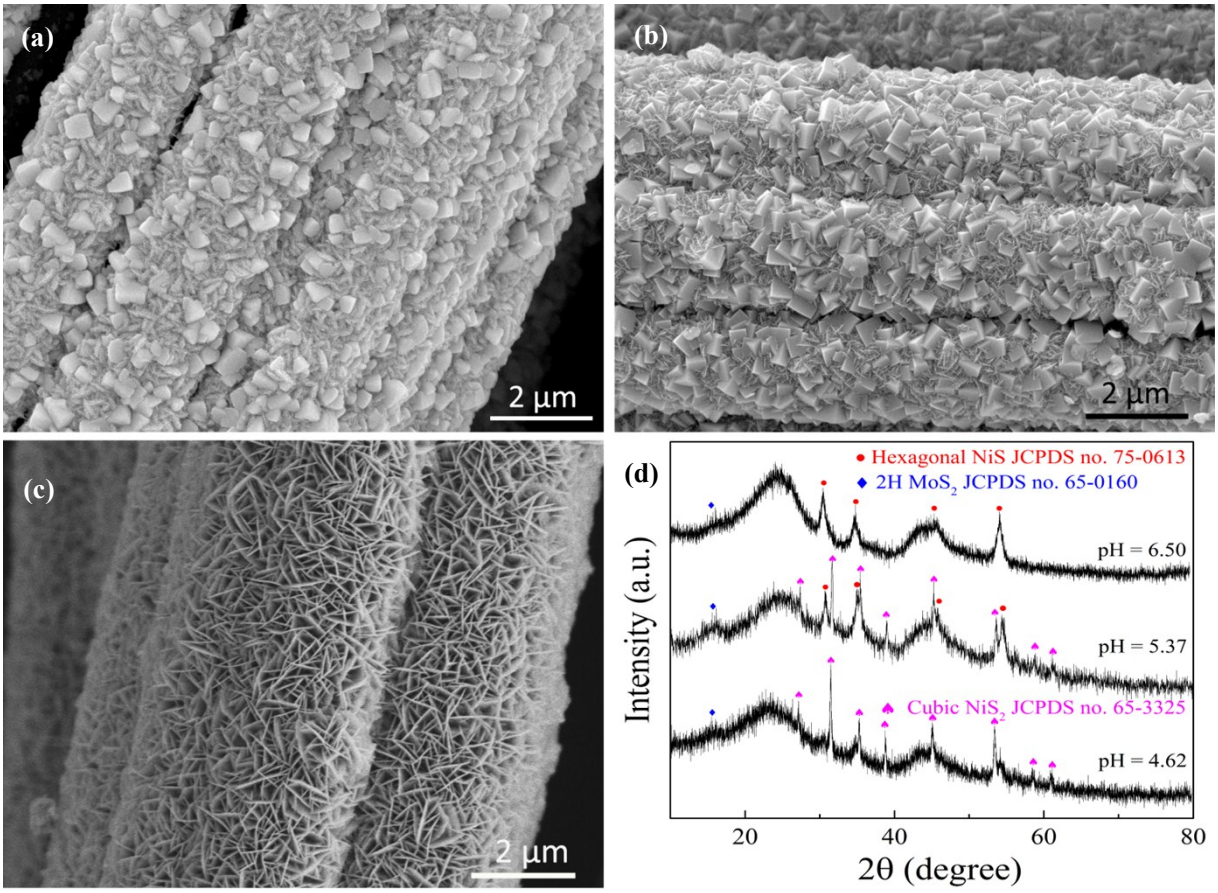

Fig. S3 SEM images of NiS-MoS_2 nanostructures on CC synthesized at different pH values: (a) 4.62 (adjusted by adding HCl), (b) 5.37 (pristine solution) and (c) 6.50 (adjusted by adding NaOH). (d) Their corresponding XRD patterns.

As shown in **Fig. S3a-b**, under acidic conditions, many cubic particles were formed. But under alkaline conditions, a plenty of vertically aligned nanosheets were obtained (**Fig. S3c**). From **Fig. S3d**, it can be seen that, as the reaction solution was changed from acid to nearly near-neutral, the phase of nickel sulfide would be transformed from cubic NiS_2 to hexagonal NiS, while that of MoS_2 would not be varied. These results reveal that a nearly neutral condition could facilitate the formation of hexagonal NiS nanosheets, but an acidic one could be beneficial for the formation of cubic NiS_2 nanoparticles.

Shundong Guan, et al., *Sustainable Energy & Fuels*, Fig. S4

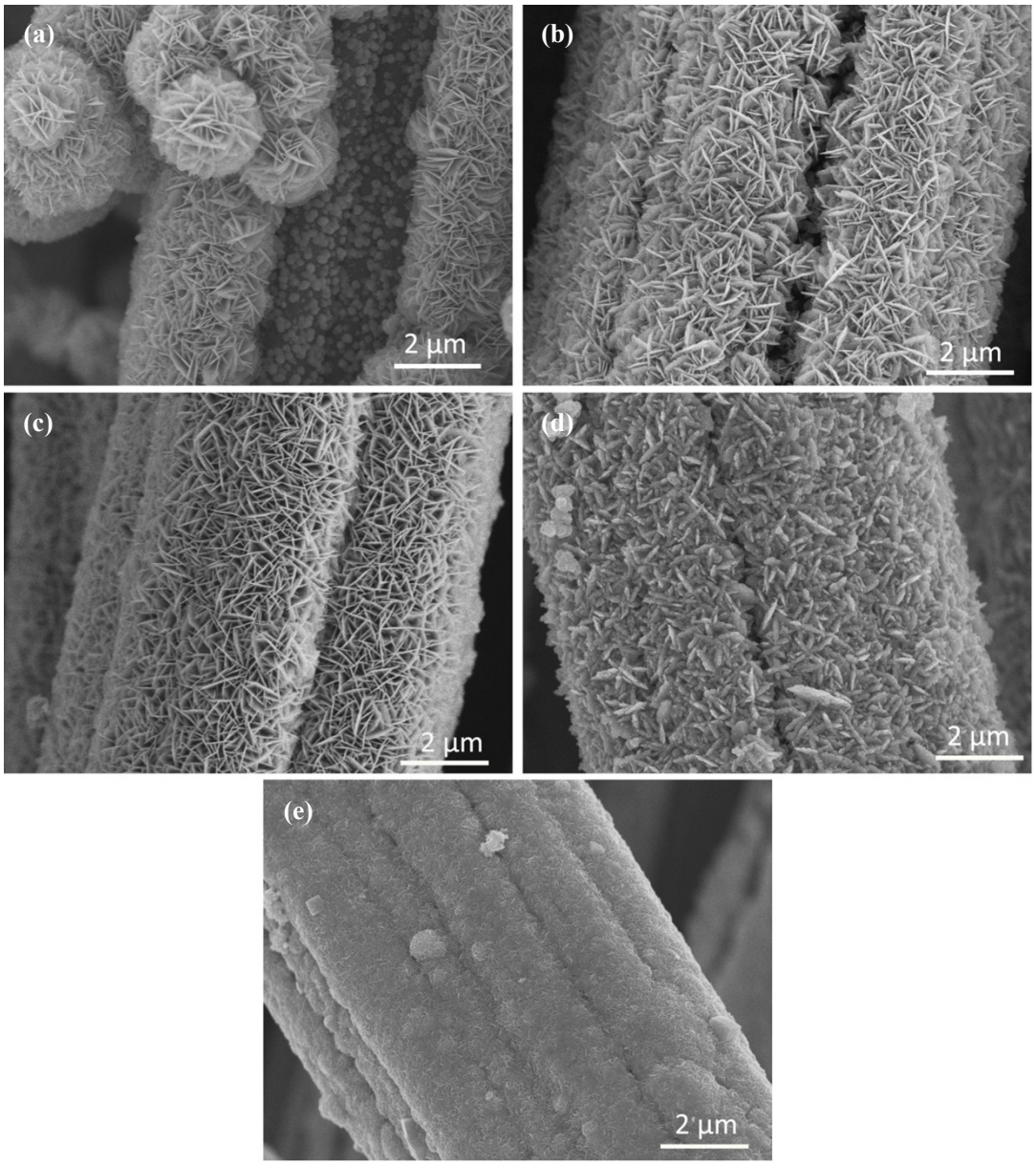

Fig. S4 SEM images of NiS-MoS_2 nanostructures on CC synthesized with different Mo/Ni feed molar ratios: (a) 0.23, (b) 0.47, (c) 0.7, (d) 0.93 and (e) 1.4.

As is seen from **Fig. S4**, when a small Mo/Ni feed molar ratio (0.23-0.47) was applied for the growth of NiS-MoS_2 nanostructures, the coating of catalysts was neither complete nor uniform on the CC. However, when a large Mo/Ni feed molar ratio (0.93-1.4) was utilized, the structure became too dense and the size of nanosheets was reduced. Thus, a moderate Mo/Ni feed molar ratio of 0.7 was selected for the growth of uniform NiS-MoS_2 HNSAs.

Shundong Guan, et al., *Sustainable Energy & Fuels*, Fig. S5

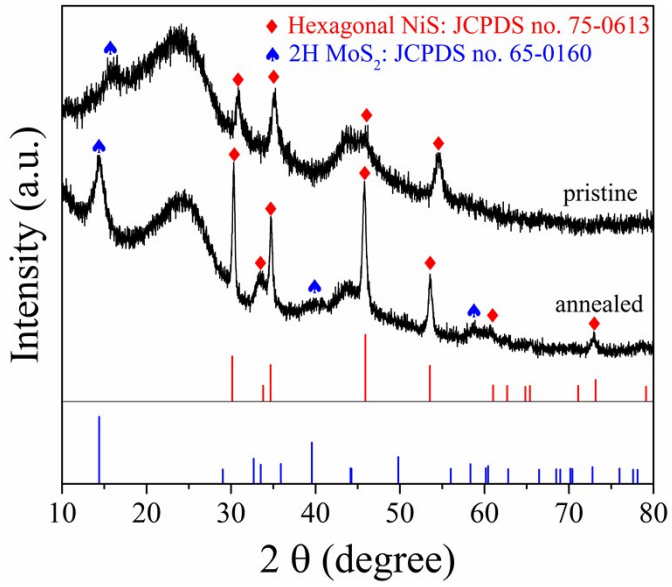

Fig. S5 XRD patterns of the NiS-MoS_2 HNSAs/CC before and after annealing.

From **Fig. S5**, it can be seen that after a simple annealing at 500 ˚C in N_2 atmosphere, all the diffraction peaks of the prepared NiS-MoS_2 HNSAs/CC became sharper than those of the pristine sample, which are matching better with the standard XRD patterns of NiS (JCPDS no. 75-0613) and MoS_2 (JCPDS no. 65-0160). These results indicate that the crystallinity of NiS-MoS_2 HNSAs/CC could be improved after annealing.

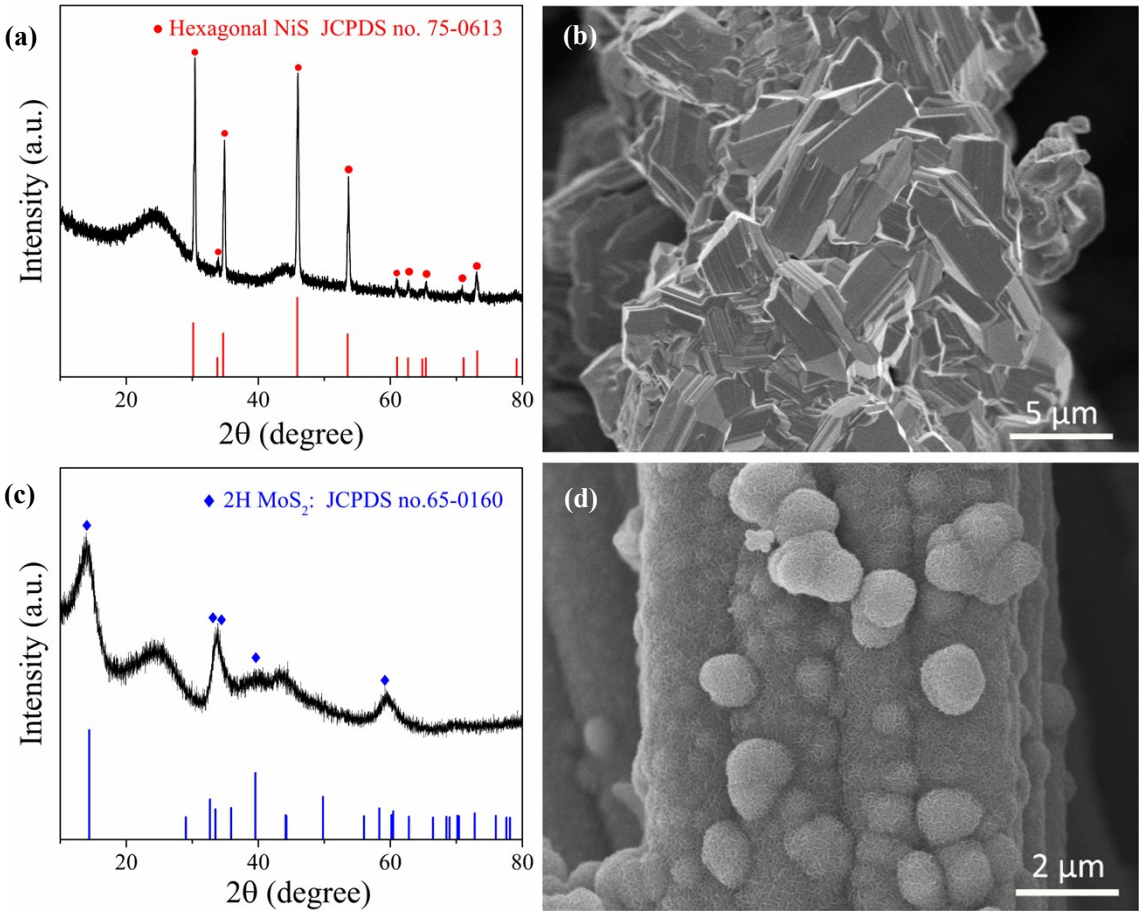

Fig. S6 XRD patterns, and the corresponding SEM images of pure NiS (a, b) and pure MoS_2 (c, d) nanostructures on the CC.

As comparative samples for NiS-MoS_2 HNSAs, pure NiS and MoS_2 were also grown on CC *via* a similar process, respectively, and then annealed under the same conditions. **Fig. S6a** indicates that the obtained NiS nanostructures are of pure hexagonal NiS phase, and **Fig. S6b** reveals that many large nanoparticles with a diameter more than 3 μm were aggregated together, wrapping the CC. These results confirm the robust growth of NiS in the absence of restrictive effect due to the growth of MoS_2. For the pure MoS_2 sample, all the diffraction peaks can be indexed to those of 2H MoS_2 phase, and the wide peaks indicate the relatively poor crystallinity of MoS_2 (**Fig. S6c**). Moreover, a layer of tiny nanosheets is uniformly coating the CC, revealing that the MoS_2 nanostructured sheets couldn't grow larger without the presence of NiS (**Fig. S6d**). Thus, the synthesis of the present NiS-MoS_2 HNSAs should be controlled by a collaborative growth process between NiS and MoS_2.

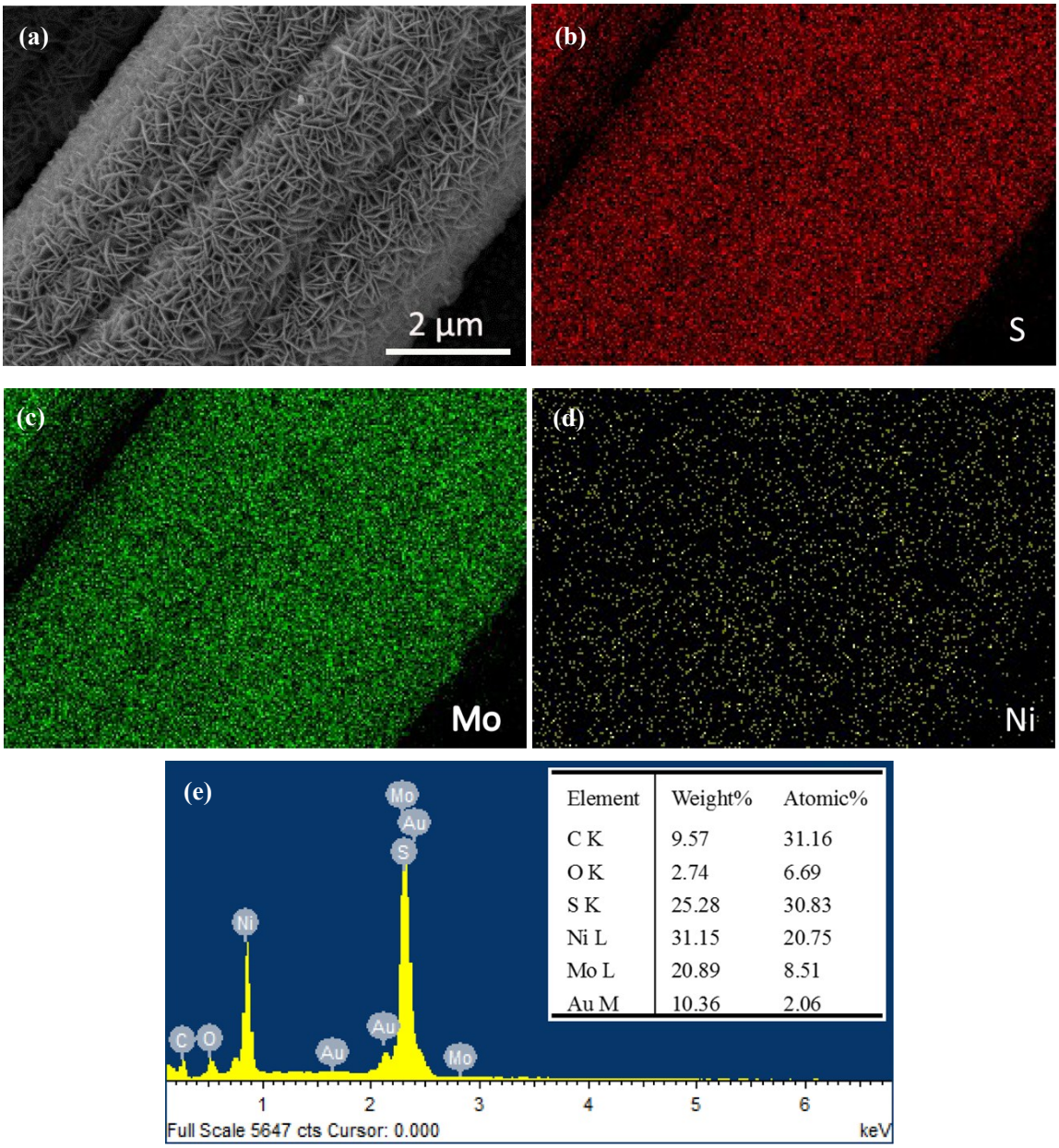

Fig. S7 EDX results. (a) Typical SEM image and the corresponding mapping spectra of S (b), Mo (c) and Ni (d) elements. (e) EDX spectrum of the NiS-MoS_2 HNSAs/CC, in which the inset is the table of element contents.

From **Fig. S7**, it can be seen that S, Mo and Ni elements are all existing over the whole surface of carbon fiber, indicating that NiS and MoS_2 are uniformly distributing on the carbon cloth (CC). It should be noted that, for the EDX spectrum, Au atoms originate from the sprayed gold during the preparation of SEM samples; and O atoms might be derived from the adsorbed O_2 or H_2O on the sample. In addition, the molar percentage of MoS_2 in the prepared NiS-MoS_2 heterostructures was calculated as about 29.1%.

Shundong Guan, et al., *Sustainable Energy & Fuels*, Fig. S8

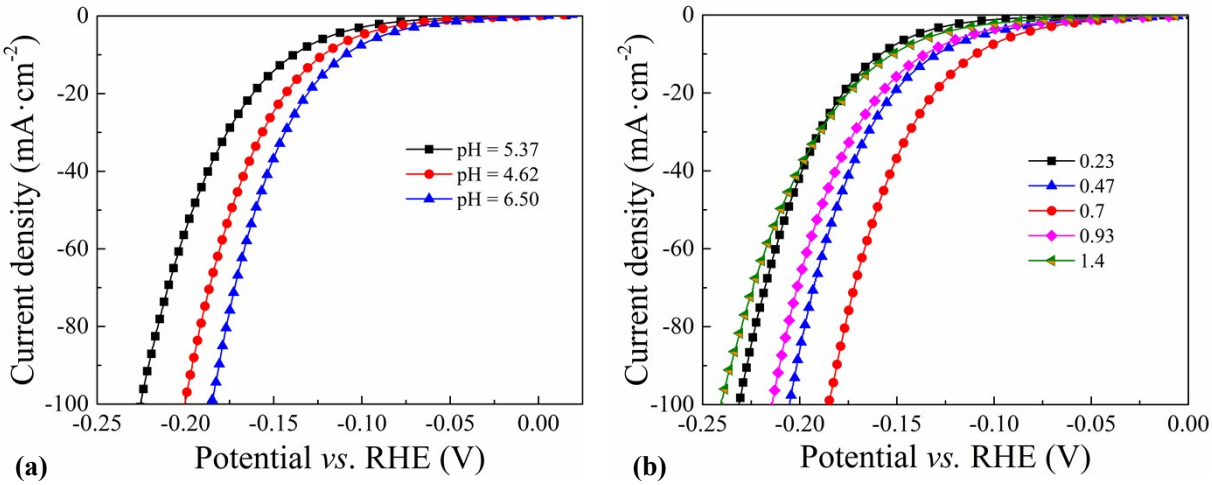

Fig. S8 Polarization curves of NiS-MoS_2 nanostructures on CC synthesized at different pH values (a) and with different Mo/Ni feed molar ratios (b), respectively. Electrolyte: 1 mol·L^{-1} KOH aqueous solution; and scan rate: 5 mV·s^{-1}.

From **Fig. S8**, it can be seen that, the NiS-MoS_2 nanostructures on CC synthesized under the optimal conditions (at pH = 6.50 and with a Mo/Ni feed molar ratio of 0.7) present the highest performance for hydrogen evolution reaction (HER).

Shundong Guan, et al., *Sustainable Energy & Fuels*, Fig. S9

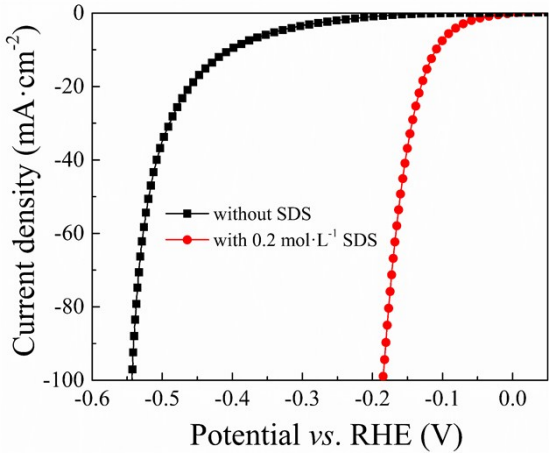

Fig. S9 Polarization curves of NiS-MoS_2 nanostructures on CC synthesized with and without SDS. Electrolyte: 1 mol·L^{-1} KOH aqueous solution; and scan rate: 5 mV·s^{-1}.

It is seen that the NiS-MoS_2/CC composite synthesized without SDS shows a much higher overpotential for HER than the heterostructures fabricated with 0.2 mol·L^{-1} SDS, probably because without the assistance of SDS, the NiS and MoS_2 couldn't effectively and uniformly grown on to the CC substrate. As a result, the product couldn't provide enough electrochemical active species for efficient HER.

Shundong Guan, et al., *Sustainable Energy & Fuels*, Fig. S10

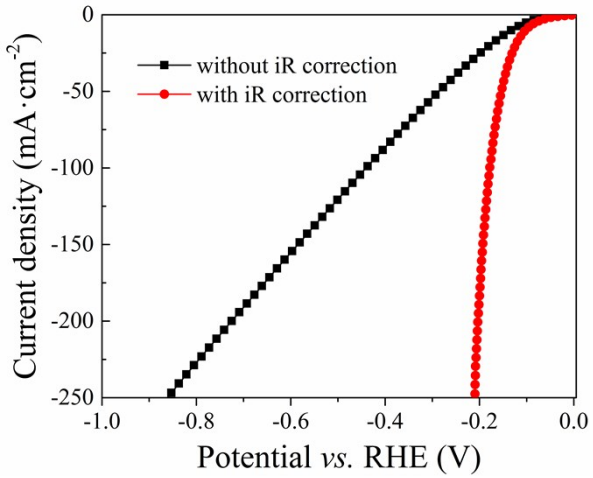

Fig. S10 Polarization curves of the present NiS-MoS_2 HNSAs/CC in 1 mol·L^{-1} KOH aqueous solution with and without *iR* correction.

From the polarization curve without *iR* correction, it can be calculated that the overpotentials at a current density of -10 and -250 mA·cm^{-1} are about 135 and 860 mV, respectively. After the *iR* correction, the cathodic current goes up sharply with the increase of applied potential, and the overpotentials at the current density of -10 and -250 mA·cm^{-1} are dramatically decreased to 106 and 200 mV, respectively.

Shundong Guan, et al., *Sustainable Energy & Fuels*, Fig. S11

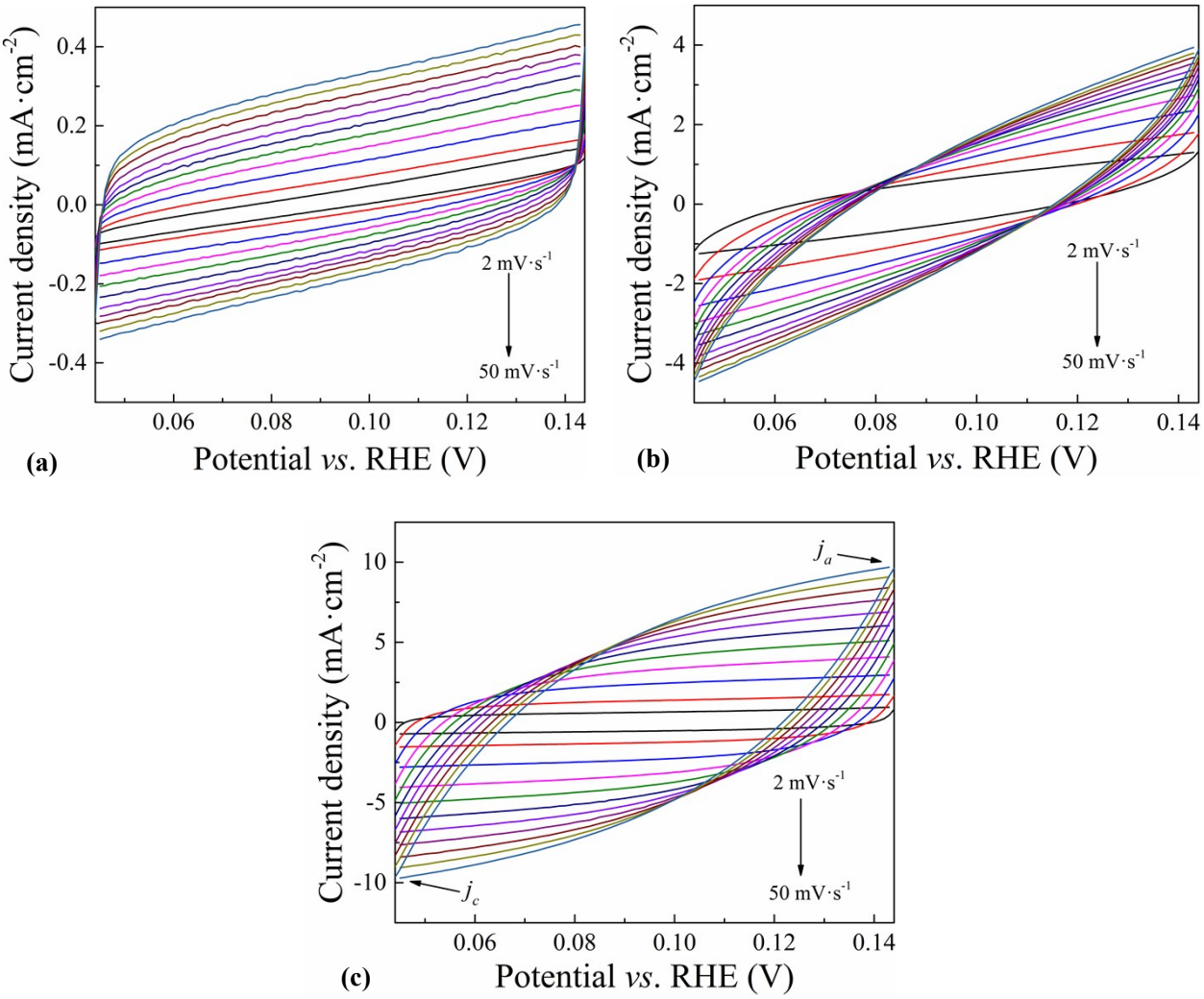

Fig. S11 Cyclic voltammograms of (a) NiS NPs/CC, (b) MoS_2 NSs/CC and (c) NiS-MoS_2 HNSAs/CC in a potential range near the HER. Electrolyte: 1 mol·L^{-1} KOH aqueous solution.

In order to estimate the HER-related electrochemical active surface area (EASA) of NiS NPs/CC, MoS_2 NSs/CC and NiS-MoS_2 HNSAs/CC, the CV curves were swept at a potential range of no faradic processes in different scan rates. The current densities at the average potential ($\Delta j/2 = (j_a - j_c)/2$) in the selected range were plotted as a function of the scan rate, and the slope of the linear fit could be calculated as the C_{dl}. From **Fig. S11**, it is seen that the NiS-MoS_2 HNSAs/CC shows larger j_a and j_c values than the NiS NPs/CC and MoS_2 NSs/CC, implying that the NiS-MoS_2 HNSAs/CC possesses the largest C_{dl} value and thus the largest EASA.

Shundong Guan, et al., *Sustainable Energy & Fuels*, Fig. S12

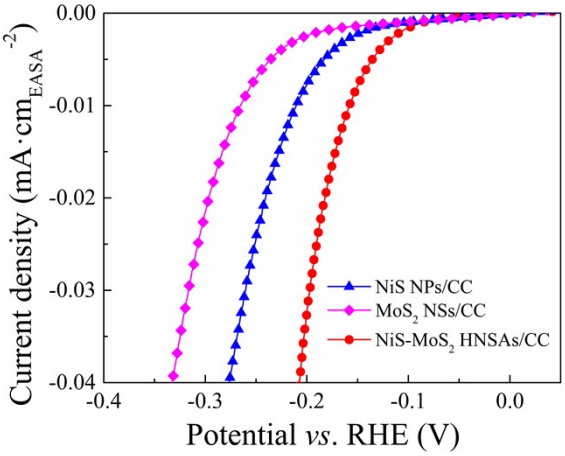

Fig. S12 Polarization curves of the NiS NPs/CC, MoS_2 NSs/CC and NiS-MoS_2 HNSAs/CC after normalizing the current by the corresponding EASA.

The specific HER activity of the samples could be estimated by normalizing the current by the corresponding EASA. From **Fig. S12**, it can be seen that the NiS-MoS_2 HNSAs/CC exhibits the lowest overpotential for HER among these three samples, indicating its highest intrinsic HER activity. Interestingly, being different from the polarization curves shown in Fig. 4a, the NiS NPs/CC shows better performance for HER than the MoS_2 NSs/CC after normalization. This result suggests that there would be much more active sites on the NiS NPs/CC as compared to those on the MoS_2 NSs/CC with the same EASA, which might be owing to the fact that the active sites of MoS_2 only exist in its edge domain.

Shundong Guan, et al., *Sustainable Energy & Fuels*, Fig. S13

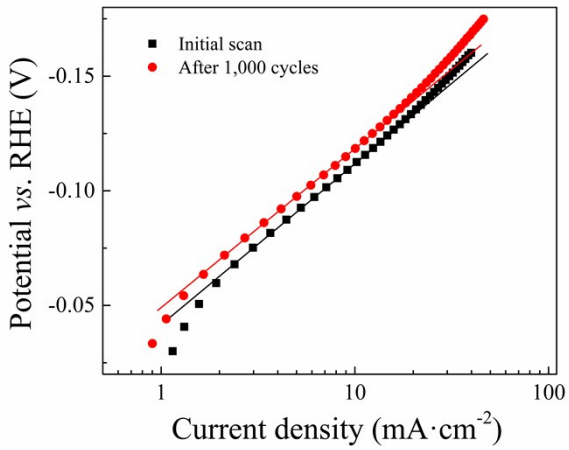

Fig. S13 Tafel plots of the NiS-MoS_2 HNSAs/CC before and after 1,000 CV scans for HER.

From this figure, it is seen that after 1,000 CV scans for HER, the Tafel slope of the NiS-MoS_2 HNSAs/CC almost equals to that of the initial scan, indicating that the mechanism for HER is not changed during 1,000 cycles, implying that the composition of the NiS-MoS_2 HNSAs/CC presents no change after this cycling test. Therefore, the slight increase of the overpotential for HER might be caused by the structure failure of the catalysts.

Shundong Guan, et al., *Sustainable Energy & Fuels*, Fig. S14

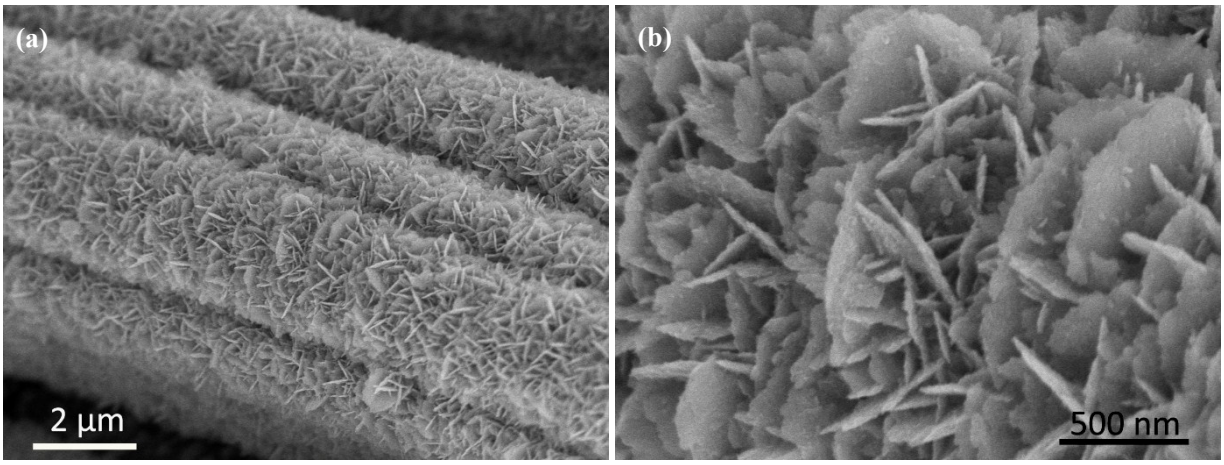

Fig. S14 Microstructure after HER test. (a) Low- and (b) high-magnification SEM images of NiS-MoS_2 HNSAs/CC after 24 h electrocatalytic HER. Electrolyte: 1 mol·L^{-1} KOH aqueous solution; and current density: -10 mA·cm^{-2}.

It can be seen from **Fig. S14** that after a long-term electrocatalytic HER test (24 h), there are no significant changes in morphology for the present NiS-MoS_2 HNSAs/CC.

Shundong Guan, et al., *Sustainable Energy & Fuels*, Fig. S15

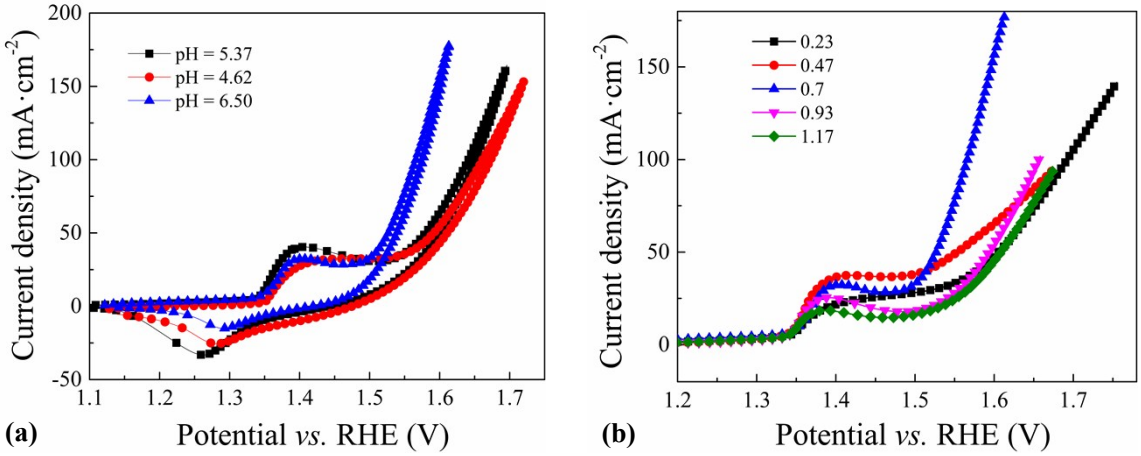

Fig. S15 CV curves of the NiS-MoS_2 nanostructures on CC synthesized at different pH values (a) and with different Mo/Ni feed molar ratios (b), respectively. Electrolyte: 1 mol·L^{-1} KOH aqueous solution; and scan rate: 5 mV·s^{-1}.

Shundong Guan, et al., *Sustainable Energy & Fuels*, Fig. S16

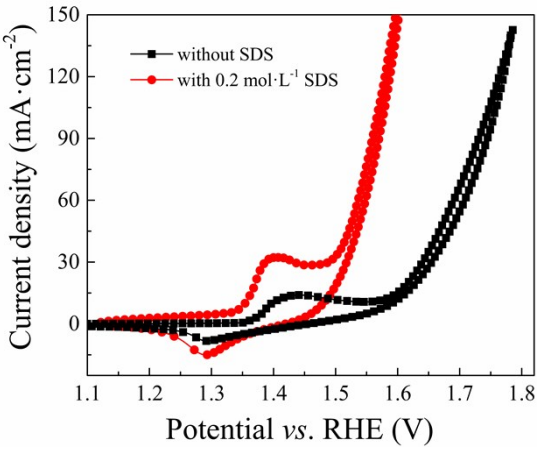

Fig. S16 CV curves of the NiS-MoS_2 nanostructures on CC synthesized with and without SDS. Electrolyte: 1 mol·L^{-1} KOH aqueous solution; and scan rate: 5 mV·s^{-1}.

As shown in **Fig. S15** and **S16**, the NiS-MoS_2/CC nanostructures synthesized under the optimal conditions (pH = 6.50, SDS = 0.2 mol·L^{-1} and Mo/Ni feed molar ratio of 0.7) present the highest performance for oxygen evolution reaction (OER), which is similar with the case for HER.

Shundong Guan, et al., *Sustainable Energy & Fuels*, Fig. S17

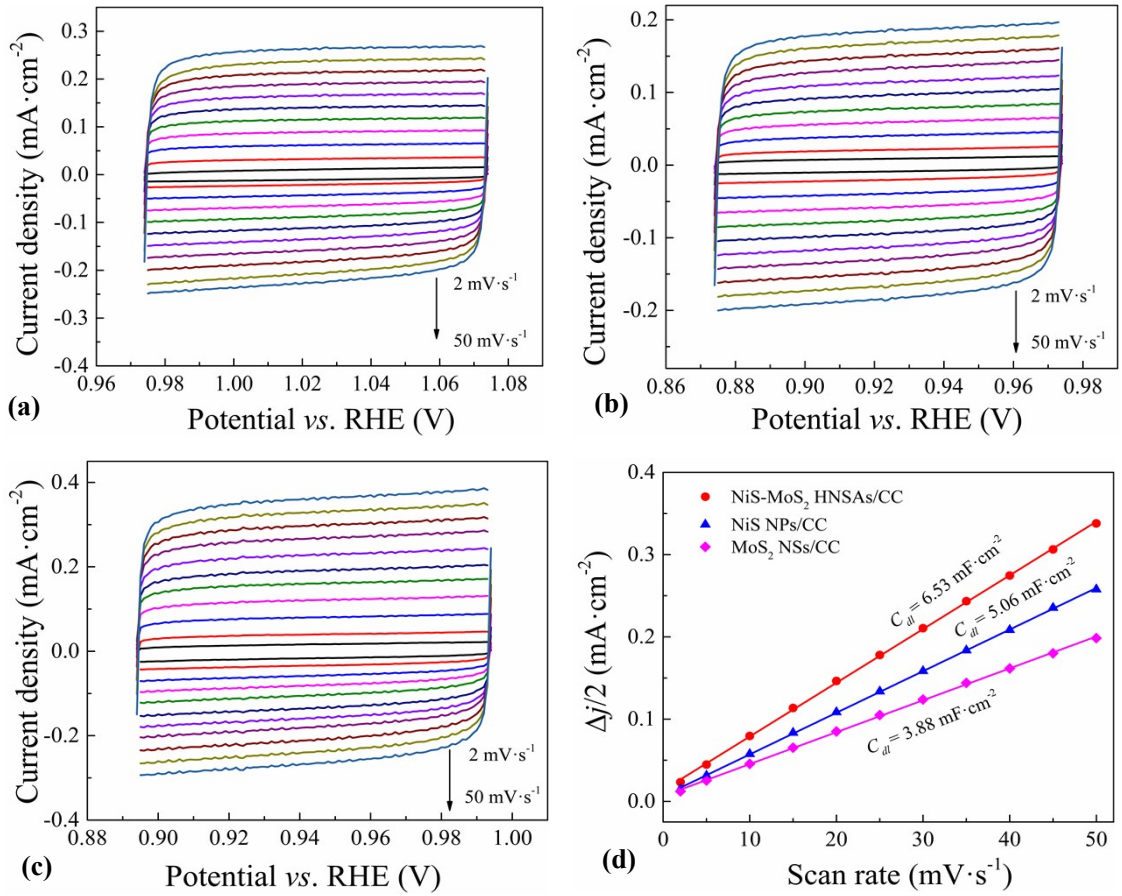

Fig. S17 Estimation of the OER-related EASA. Cyclic voltammograms of NiS NPs/CC (a), MoS_2 NSs/CC (b) and NiS-MoS_2 HNSAs/CC (c) in a potential range near the OER. (d) The fitting plots of C_{dl} for the three samples.

Similar with the HER test, the OER-related EASA value of the catalysts can be also evaluated *via* the CV curves by selecting the potential range for OER without the faradic processes. From the CV curves shown in **Fig. S17a-c**, the C_{dl} values of the NiS NPs/CC, MoS_2 NSs/CC and NiS-MoS_2 HNSAs/CC were calculated as 5.06, 3.88 and 6.53 mF·cm^{-2} (**Fig. S17d**), corresponding to their EASA values of 126.5, 91.0 and 163.2 cm^2, respectively. The NiS-MoS_2 HNSAs/CC has the highest EASA value, indicating its highest specific surface area.

Shundong Guan, et al., *Sustainable Energy & Fuels*, Fig. S18

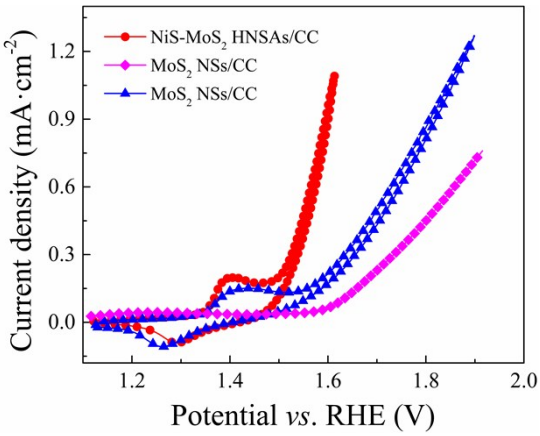

Fig. S18 CV curves of the NiS NPs/CC, MoS_2 NSs/CC and NiS-MoS_2 HNSAs/CC after normalizing the current by the corresponding EASA.

It is seen that even if the current is normalized by the corresponding EASA, the performance of the NiS-MoS_2 HNSAs/CC is still significantly better than its counterparts (the NiS NPs/CC and MoS_2 NSs/CC), suggesting the highest intrinsic OER activity of such NiS-MoS_2 heterogeneous nanostructures.

Shundong Guan, et al., *Sustainable Energy & Fuels*, Fig. S19

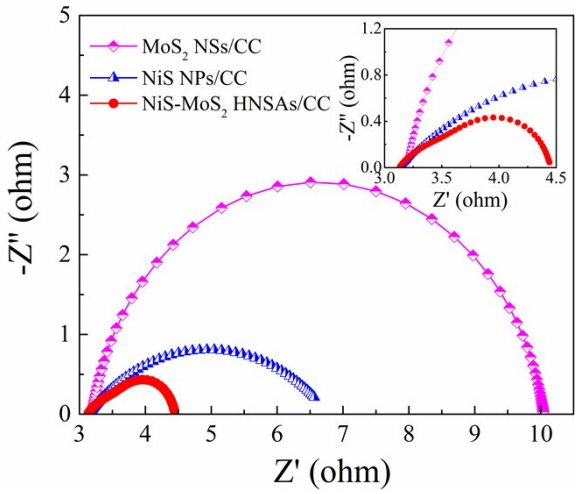

Fig. S19 EIS Nyquist plots of NiS NPs/CC, MoS_2 NSs/CC and NiS-MoS_2 HNSAs/CC for OER, where the inset shows the enlarged view at the range of high frequency. Electrolyte: 1 mol·L^{-1} KOH aqueous solution. And the results were measured at 0.75 V *vs*. Hg/HgO.

From **Fig. S19** it can be seen that, all the electrodes show small and similar series resistance (R_s) about 3.2 Ohm; but the present NiS-MoS_2 HNSAs/CC possesses the lowest charge transfer resistance (R_{ct}). This result indicates the fastest electrochemical reaction rate on the surface of NiS-MoS_2 HNSAs/CC. Furthermore, similar with the EIS Nyquist plots for HER, two capacitive semicircles with different curvatures are also displayed in the present NiS-MoS_2 HNSAs/CC, revealing that there are two different electrochemical reaction surfaces (NiS and MoS_2) during the OER process. And both capacitive semicircles show a lower R_{ct} than those of NiS NPs/CC and MoS_2 NSs/CC, suggesting there is a synergistic effect between NiS and MoS_2.

Shundong Guan, et al., *Sustainable Energy & Fuels*, Fig. S20

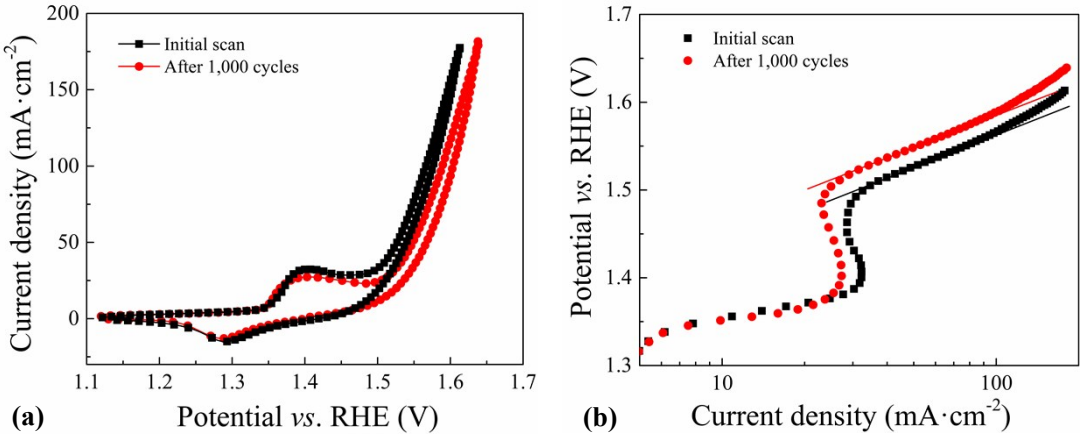

Fig. S20 CV curves (a) and Tafel plots (b) of the NiS-MoS_2 HNSAs/CC before and after 1,000 cycles for OER.

Similar with the HER test, only a slight increase (< 10%) in overpotential could be detected after 1,000 cycles test for OER, and the Tafel slope was almost kept as that in the initial scan, revealing an excellent cycling stability of the NiS-MoS_2 HNSAs/CC for OER.

Shundong Guan, et al., *Sustainable Energy & Fuels*, Fig. S21

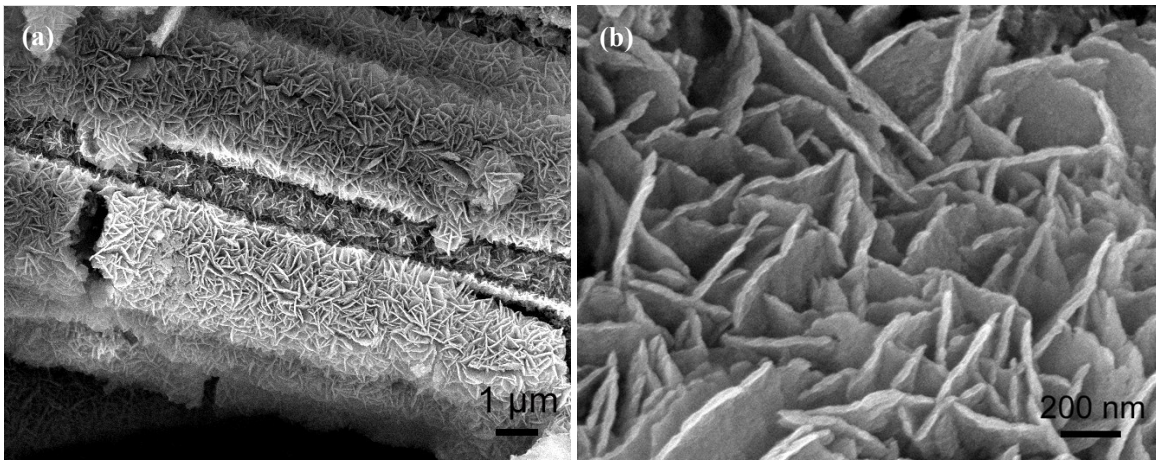

Fig. S21 Microstructure after OER test. (a) Low- and (b) high-magnification SEM images of NiS-MoS_2 HNSAs/CC after 24 h electrocatalytic OER test. Electrolyte: 1 mol·L^{-1} KOH aqueous solution; and current density: 10 mA·cm^{-2}.

From **Fig. S21**, it can be seen that despite of the drastic redox reaction over NiS during the OER process, the morphology of the NiS-MoS_2 HNSAs catalyst was changed slightly after a long-term test (24 h). The diameter of a single fiber might be expanded somewhat, but the aligned structure of the nanosheets was changed very little.

Table S1. Elemental contents on the surface of the NiS-MoS_2 HNSAs/CC (detected by XPS)

Elements	At.%
S 2p	26.084
Mo3d S2s	15.306
C 1s	29.776
O 1s	22.868
Ni 2p	5.966

Shundong Guan, et al., *Sustainable Energy & Fuels*, Table S2

Table S2. Comparison on the HER performance of the present NiS-MoS_2 HNSAs/CC with other reported noble-metal free electrocatalysts in alkaline media

Catalysts[a]	η_{10} (mV)	η_{onset} (mV)	Tafel slope (mV·dec^{-1})	Electrolyte[b]	Ref.
NiS-MoS_2 HNSAs/CC	106	51	56.7	1.0 M KOH	This work
$NiFeO_x$ on carbon fiber paper	88	40	150	1.0 M KOH	7
Porous MoO_2 nanosheets/NF	27	~ 0	41	1.0 M KOH	8
Amorphous Ni-Co complexes with 1T phase MoS_2	70	-	38.1	1.0 M KOH	14
NiS_2/MoS_2 hybrid nanowire	204	134	65	1.0 M KOH	17
Ni_3S_2 nanosheet arrays/NF	223	-	-	1.0 M NaOH	21
MoS_2/Ni_3S_2 nanostructures /NF	110	50	83	1.0 M KOH	22
MoS_2-Ni_3S_2 heteronanorods/NF	98	31	61	1.0 M KOH	23
MoS_2/NiS nanocuboids/NF	92	-	113	1.0 M KOH	24
NiSe nanowires/NF	96	-	120	1.0 M KOH	S1
Ni-Fe/nitrogen doped nanocarbon	219	-	101	1.0 M KOH	S2
Mo_2N–Mo_2C/HGr	154	18	68	1.0 M KOH	S3
NiCu@C	94	-	74	-	S4
Ni_2P@NPCNFs	104.2	-	79.7	1.0 M KOH	S5
CP/CTs/Co-S	190	-	131	1.0 M KOH	S6
NiMo HNRs/Ti mesh	92	60	76	1.0 M KOH	S7
$NiCo_2O_4$ hollow microcuboids	110	50	49.7	1.0 M NaOH	S8
Co/N, B-doped carbon	183	-	73.2	1.0 M KOH	S9
N-doped porous MoC nanobelts	110	52	49.7	1.0 M KOH	S10

a) C: carbon; NF: nickel foam

b) M: mol·L^{-1}

Shundong Guan, et al., *Sustainable Energy & Fuels*, Table S3

Table S3. Comparison on the OER performance of the present NiS-MoS_2 HNSAs/CC with other reported noble-metal free electrocatalysts in alkaline media

Catalysts	η_{10} (mV)	Tafel slope ($mV \cdot dec^{-1}$)	Electrolyte	Ref.
NiS-MoS_2 HNSAs/CC	203	77.4	1.0 M KOH	This work
$NiFeO_x$/CFP	~ 230	31.5	1.0 M KOH	7
Porous MoO_2 nanosheets/NF	260	54	1.0 M KOH	8
Amorphous Ni-Co complexes with 1T phase MoS_2	235	45.7	1.0 M KOH	14
Ni_3S_2 nanosheet arrays /NF	260	-	1.0 M NaOH	21
MoS_2/Ni_3S_2 nanostructures/ NF	218	88	1.0 M KOH	22
MoS_2-Ni_3S_2 heteronanorods/NF	249	66	1.0 M KOH	23
MoS_2/NiS nanocuboids/NF	271@η_{15}	53	1.0 M KOH	24
Ni-Fe/nitrogen doped nanocarbon	330	45	1.0 M KOH	S2
CP/CTs/Co-S	306	72	1.0 M KOH	S6
NiMo HNRs/Ti mesh	310	47	1.0 M KOH	S7
$NiCo_2O_4$ hollow microcuboids	290	53	1.0 M NaOH	S8
Ni_3S_2 nanorods/NF	187	157	0.1 M KOH	S11
NiFe LDHs	~300	40	1.0 M KOH	S12
Fe decorated porous Ni-Cd	290	38	0.1 M NaOH	S13
Ni-MnO/rGO	370	67	0.1 M KOH	S14
Fe/$Ni_{2.4}$/$Co_{0.4}$-MIL-53	219	53.5	1.0 M KOH	S15
Ni-Fe LDH hollow nanoprism	280	49.4	1.0 M KOH	S16

Shundong Guan, et al., *Sustainable Energy & Fuels*, Table S4

Table S4. Comparison on the overall water splitting performance of the present NiS-MoS_2 HNSAs/CC with recently reported noble-metal free bi-functional electrocatalysts in alkaline media

Catalysts	HER η_{10} (mV)	OER η_{10} (mV)	Overall water splitting cell voltage (V, at 10 mA·cm^{-2})	Electrolyte	Ref.
NiS-MoS_2 HNSAs/CC	106	203	1.54	1.0 M KOH	This work
$NiFeO_x$/CFP	88	~230	1.51	1.0 M KOH	7
Porous MoO_2 nanosheets/NF	27	260	1.52	1.0 M KOH	8
Amorphous Ni-Co complexes with 1T phase MoS_2	70	235	1.48	1.0 M KOH	14
NiS microspheres film/NF	-	-	1.64	1.0 M KOH	19
Ni_3S_2 nanosheet arrays/NF	223	260	~1.76	1.0 M NaOH	21
MoS_2/Ni_3S_2 nanostructures/NF	110	218	1.56	1.0 M KOH	22
MoS_2-Ni_3S_2 heteronanorods/NF	98	249	1.50	1.0 M KOH	23
MoS_2/NiS nanocuboids/NF	92	271@η_{15}	1.61	1.0 M KOH	24
Ni_3N-NiMoN heterostructures	31	277	1.54	1.0 M KOH	47
Ni-Fe-O nanowire network	-	244	1.64	1.0 M KOH	48
NiSe nanowires/NF	96	-	1.63	1.0 M KOH	S1
Ni-Fe/nitrogen doped nanocarbon	219	330	1.58	1.0 M KOH	S2
CP/CTs/Co-S	190	306	1.743	1.0 M KOH	S6
NiMo HNRs/Ti mesh	92	310	1.64	1.0 M KOH	S7
$NiCo_2O_4$ hollow microcuboids	110	290	1.65	1.0 M NaOH	S8
CoP/NCNHP	115	310	1.64	1.0 M KOH	S17
Ni_3N-NiMoN heterostructures	31	277	1.54	1.0 M KOH	S18

Shundong Guan, et al., *Sustainable Energy & Fuels*, Table S5

Table S5. The theoretical amounts, measured amounts and Faradaic efficiencies of HER and OER at different stages over the NiS-MoS_2 HNSAs/CC.

Time (min)	Theoretical amount (μmol)		Measured amount (μmol)		Faraday efficiency (%)	
	HER	OER	HER	OER	HER	OER
5	15.55	7.77	14.35	6.98	92.3	89.8
10	31.09	15.55	30.63	14.36	98.5	92.3
15	46.64	23.32	46.53	21.54	99.8	92.4
20	62.18	31.09	61.92	28.78	99.6	92.6
25	77.73	38.87	76.62	36.13	98.6	93
30	93.28	46.64	92.69	43.12	99.4	92.4
35	108.82	54.41	108.46	50.68	99.7	93.1
40	124.37	62.18	123.58	57.99	99.4	93.3
45	139.92	69.96	139.78	65.38	99.9	93.4
50	155.46	77.73	155.16	72.17	99.8	92.8
55	171.01	85.5	169.66	79.74	99.2	93.3
60	186.56	93.27	186.05	87.18	99.7	93.5

Note S1. Calculations of Faraday efficiency

Firstly, the theoretical value (V_T) of H_2 and O_2 can be calculated based on the following formula,

$$V_T = \frac{I \times t}{F \times n_e} \quad \text{(S1)}$$

where I is the current (A) applied on the electrodes, t is the reaction time (s), and F is the Faraday constant. And n_e is the transferred electron number corresponding to the generation of every H_2 or O_2 molecule, which can be determined by the water splitting reactions in alkaline solution,[9]

H_2 on cathode: $2H_2O + 2e^- \rightarrow H_2 + 2OH^-$ (S2)

O_2 on anode: $4OH^- \rightarrow 2H_2O + O_2 + 4e^-$ (S3)

Thus, the n_e values for H_2 and O_2 are 2 and 4, respectively.

Finally, the Faraday efficiency (e_F) can be calculated using the following formula,

$$e_F = \frac{V_M}{V_T} \times 100\% \quad \text{(S4)}$$

in which, V_M is the measured amount of H_2 or O_2.

References

S1 C. Tang, N. Y. Cheng, Z. H. Pu, W. Xing and X. P. Sun, *Angew. Chem. Int. Edit.*, 2015, **54**, 9351-9355.

S2 X. Zhang, H. M. Xu, X. X. Li, Y. Y. Li, T. B. Yang and Y. Y. Liang, *ACS Catal.*, 2016, **6**, 580-588.

S3 H. J. Yan, Y. Xie, Y. Q. Jiao, A. P. Wu, C. G. Tian, X. M. Zhang, L. Wang and H. G. Fu, *Adv. Mater.*, 2018, **30**, 1704156.

S4 Y. Shen, Y. F. Zhou, D. Wang, X. Wu, J. Li and J. Y. Xi, *Adv. Energy Mater.*, 2018, **8**, 1701759.

S5 M. Q. Wang, C. Ye, H. Liu, M. W. Xu and S. J. Bao, *Angew. Chem. Int. Edit.*, 2018, **57**, 1963-1967.

S6 J. Wang, H. X. Zhong, Z. L. Wang, F. L. Meng and X. B. Zhang, *ACS Nano*, 2016, **10**, 2342-2348.

S7 J. Q. Tian, N. Y. Cheng, Q. Liu, X. P. Sun, Y. Q. He and A. M. Asiri, *J. Mater. Chem. A*, 2015, **3**, 20056-20059.

S8 X. H. Gao, H. X. Zhang, Q. G. Li, X. G. Yu, Z. L. Hong, X. W. Zhang, C. D. Liang and Z. Lin, *Angew. Chem. Int. Edit.*, 2016, **55**, 6290-6294.

S9 H. B. Zhang, Z. J. Ma, J. J. Duan, H. M. Liu, G. G. Liu, T. Wang, K. Chang, M. Li, L. Shi, X. G. Meng, K. C. Wu and J. H. Ye, *ACS Nano*, 2016, **10**, 684-694.

S10 S. Y. Jing, L. S. Zhang, L. Luo, J. J. Lu, S. B. Yin, P. K. Shen and P. Tsiakaras, *Appl. Catal. B-Environ.*, 2018, **224**, 533-540.

S11 W. J. Zhou, X. J. Wu, X. H. Cao, X. Huang, C. L. Tan, J. Tian, H. Liu, J. Y. Wang and H. Zhang, *Energy Environ. Sci.*, 2013, **6**, 2921-2924.

S12 F. Song and X. L. Hu, *Nat. Commun.*, 2014, **5**, 4477.

S13 J. H. Kim, D. H. Youn, K. Kawashima, J. Lin, H. Lim and C. B. Mullins, *Appl. Catal. B-Environ.*, 2018, **225**, 1-7.

S14 G. T. Fu, X. X. Yan, Y. F. Chen, L. Xu, D. M. Sun, J. M. Lee and Y. W. Tang, *Adv. Mater.*, 2018, **30**, 1704609.

S15 F. L. Li, Q. Shao, X. Q. Huang and J. P. Lang, *Angew. Chem. Int. Edit.*, 2018, **57**, 1888-1892.

S16 L. Yu, J. F. Yang, B. Y. Guan, Y. Lu and X. W. Lou, *Angew. Chem. Int. Edit.*, 2018, **57**, 172-176.

S17 Y. Pan, K. A. Sun, S. J. Liu, X. Cao, K. L. Wu, W. C. Cheong, Z. Chen, Y. Wang, Y. Li, Y. Q. Liu, D. S. Wang, Q. Peng, C. Chen and Y. D. Li, *J. Am. Chem. Soc.*, 2018, **140**, 2610-2618.

S18 A. P. Wu, Y. Xie, H. Ma, C. G. Tian, Y. Gu, H. J. Yan, X. M. Zhang, G. Y. Yang and H. G. Fu, *Nano Energy*, 2018, **44**, 353-363.